PCCP

RSC Publishing

PAPER

View Article Online
View Journal | View Issue

Cite this: *Phys. Chem. Chem. Phys.*, 2013, **15**, 11128

Probing the electrode/electrolyte interface in the lithium excess layered oxide $Li_{1.2}Ni_{0.2}Mn_{0.6}O_2$†

Kyler J. Carroll,[a] Danna Qian,[a] Chris Fell,[b] Scott Calvin,[c] Gabriel M. Veith,[d] Miaofang Chi,[d] Loic Baggetto[d] and Ying Shirley Meng*[a]

Received 7th May 2013,
Accepted 7th May 2013

DOI: 10.1039/c3cp51927a

www.rsc.org/pccp

A detailed surface investigation of the lithium-excess nickel manganese layered oxide $Li_{1.2}Ni_{0.2}Mn_{0.6}O_2$ structure was carried out using X-ray photoelectron spectroscopy (XPS), total electron yield and transmission X-ray absorption spectroscopy (XAS), and electron energy loss spectroscopy (EELS) during the first two electrochemical cycles. All spectroscopy techniques consistently showed the presence of Mn^{4+} in the pristine material and a surprising reduction of Mn at the voltage plateau during the first charge. The Mn reduction is accompanied by the oxygen loss revealed using EELS. Upon the first discharge, the Mn at the surface never fully recovers back to Mn^{4+}. The electrode/electrolyte interface of this compound consists of the reduced Mn at the crystalline defect-spinel inner layer and an oxidized Mn species simultaneously with the presence of a superoxide species in the amorphous outer layer. This proposed model signifies that oxygen vacancy formation and lithium removal result in electrolyte decomposition and superoxide formation, leading to Mn activation/dissolution and surface layer-spinel phase transformation. The results also indicate that the role of oxygen is complex and significant in contributing to the extra capacity of this class of high energy density cathode materials.

Introduction

A better understanding of the interfacial region between an electrode material and the electrolyte during battery operation is important for the design and optimization of next generation lithium ion batteries.[1] As such, this interfacial region has been extensively studied over the past decade on a variety of electrode materials. One material currently of interest is the high voltage $Li_{1.2}Ni_{0.2}Mn_{0.6}O_2$ cathode material due to its ability to deliver reversible capacities in excess of 250 mA h g^{-1} at higher operating voltages (>4.5 V).[2] The initial capacity and the resulting sloped region up to 4.40 V in the charge curve result in lithium removal and concomitantly the oxidation of Ni^{2+} to Ni^{4+} while it has been suggested that Mn^{4+} remains unchanged.[3] Following this process lithium extraction continues despite the fully charged transition metal oxidation states, and is shown by a plateau region at ~4.50 V, the mechanism of which has been a subject of discussion in recent literature.[2c,4] While this anomalous plateau results in a greater first charge capacity, it is also associated with a larger irreversibility on the first discharge of up to ~100 mA h g^{-1}; the subsequent charge curves are without this anomalous plateau region.[5] The fundamental question with these materials is what causes the large irreversible loss in capacity. There are several proposed mechanisms in the literature; for example, some attribute the loss in capacity to the electrolyte/electrode interface reaction, occurring at higher operating voltages, causing electrolyte decomposition and possible HF formation that results in transition metal leaching at the surface during the first charge.[4e,6] Other groups have attributed the capacity loss to simultaneous Li^+ and O^{2-} removal from the material, resulting in transition metal migration and rearrangement.[2c,3a,4d,6,7] Armstrong *et al.* proposed oxygen evolution from the crystal structure by examining the first charge using neutron diffraction and also analyzed the gases produced *in situ* with differential electrochemical mass spectrometry.[2c] They proposed a transition metal migration theory, which involves the formation of oxygen vacancies as a result of lithium migration at the surface of the material and subsequent transition metal migration into the lithium layer. Building on this work, more recent literature discusses the formation of a defect-like spinel phase as a result of oxygen vacancies.[4b,6] Xu *et al.* have

[a] *Department of NanoEngineering, University of California, San Diego, La Jolla, CA 92037, USA. E-mail: shirleymeng@ucsd.edu*
[b] *Department of Materials Science and Engineering, University of Florida, Gainesville, FL 32611, USA*
[c] *Department of Physics, Sarah Lawrence College, Bronxville, NY 10708, USA*
[d] *Materials Science and Technology Division, Oak Ridge National Laboratory, Oak Ridge, TN, USA*

† Electronic supplementary information (ESI) available. XPS, XAS, and EELS data can be found in the supporting information. This material is available free of charge *via* the internet at http://pubs.acs.org. See DOI: 10.1039/c3cp51927a

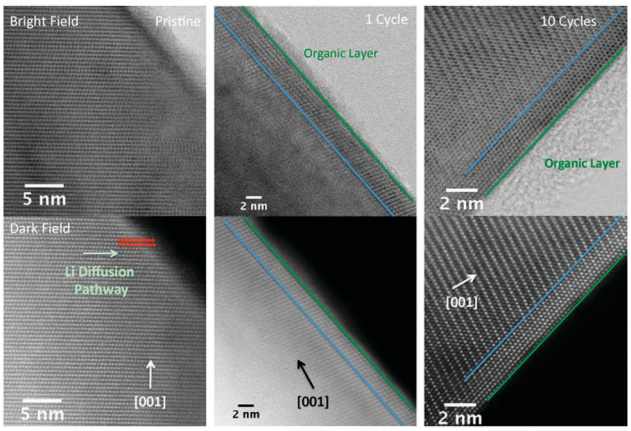

Fig. 1 a-STEM images for pristine and 1 and 10 electrochemically cycled electrode materials with their corresponding HAADF images showing surface rearrangement occurring after cycling.

shown, through electron energy loss spectroscopy (EELS), that after extended cycling the valence of Mn ions near the surface (~2–5 nm) was reduced and the oxygen K-edge pre-peak signal diminished, suggesting a change in the TM–O bonding characteristics.[4b]

Recently significant advances in microscopy, specifically the addition of spherical aberration correctors to the STEM, have allowed drastic improvements in the spatial resolution, allowing sub-angstrom resolution.[8] Fig. 1 shows visually, using scanning transmission electron microscopy (STEM) performed by the authors, after subsequent cycling cation rearrangement at the surface of the particle (a crystalline inner layer) in conjunction with an increase in the amorphous outer layer. The figure also shows successive surface cation rearrangement with extended cycling and was the motivation of this work.

While there has been extensive effort devoted to elucidating the mechanisms associated with this material, there is still a lack of clarity in understanding the origin of the anomalous capacity and its irreversible nature. More research is needed to correlate both the surface and bulk changes during the first cycle as well as examine the electrode/electrolyte interfacial reactions at the surface of the electrodes at higher operating voltages. This work focuses on answering these questions by using several surface sensitive techniques to examine the surface of the electrode material at various states of charge during the first and second cycle. X-ray photoelectron spectroscopy has been a widely used surface characterization tool for analyzing the electrode/electrolyte interfacial reactions after electrochemical cycling.[9] Typically, cycled samples are disassembled in a glove box and then transferred in air to the XPS prior to analysis. This, however, tends to lead to changes in the surface composition as the surface species tend to be highly reactive in moisture and air. Here we report a transfer technique developed at Oak Ridge National Laboratory (ORNL) that prevents samples from coming into contact with moisture and air prior to XPS analysis by using a specialized load-lock system. This system allows for a more accurate investigation of surface species present at various states of charge. In addition, total electron yield and transmission X-ray absorption spectroscopy were used in this work to investigate, simultaneously, the surface and bulk local structural changes and oxidation states of the transition metals (Ni, Mn). By combining both surface sensitive and bulk XAS techniques simultaneously we are able to more accurately correlate the oxidation state changes in both the surface and bulk of the material during electrochemical cycling. We use these two techniques combined with electron energy loss spectroscopy (EELS) and high-resolution STEM to further quantify surface changes during cycling. This work, with several highly surface sensitive characterization techniques, focuses on the transition metal migration, oxidation state changes in the bulk and the surface for Ni and Mn, and the associated oxygen vacancy formation in order to more accurately elucidate the mechanism of the first cycle capacity loss and reasons for the anomalous capacity.

Experimental section

Synthesis

A co-precipitation technique was used for the synthesis of the materials which was previously described.[5] Transition metal nitrates, $Ni(NO_3)_2{\cdot}6H_2O$ (Fisher) and $Mn(NO_3)_2{\cdot}4H_2O$ (Fisher), were titrated into a stoichiometric $LiOH{\cdot}H_2O$ (Fisher) solution for a duration of two hours. The co-precipitated transition metal hydroxides were then filtered using a vacuum filter and washed three times with deionized water. The collected transition metal hydroxides were dried in an oven at 180 °C for 10 hours in air. The dried transition metal precursors were mixed with a stoichiometric amount of $LiOH{\cdot}H_2O$ corresponding to the amount of $M(OH)_2$ from the co-precipitation step. This mixture was ground for 30 minutes to ensure adequate mixing and then placed into a furnace at 480 °C for 12 hours. The pre-calcinated powders were prepared as a pellet for high temperature sintering. These samples were then calcinated at 1000 °C for 12 hours in air. Samples were cooled in the furnace back to room temperature.

Electrochemical cells

Cathodes and electrochemical coin cells (2016) were prepared using standard procedures, the details of which have been reported elsewhere.[4a,5] Briefly, cathodes were prepared by mixing the active material $Li[Ni_xLi_{1/3-2x/3}Mn_{2/3-x/3}]O_2$ (x = 1/5) with 10 wt% Super P carbon (TIMCAL) and 10 wt% poly-vinylidene fluoride (PVDF) in *N*-methyl pyrrolidone (NMP) solution. The slurry was cast onto an Al foil using a doctor blade and dried in a vacuum oven at 80 °C overnight. The electrode discs were punched and dried again at 80 °C for 6 hrs before storing them in an argon-filled glove box (H_2O level < 1 ppm). The electrolyte solution is composed of 1 M $LiPF_6$ in a 1:1 ethylene carbonate (EC): dimethyl carbonate (DMC) solution. Cells were brought to predetermined states of charge on the first charge and discharge cycle (4.8 V–2.0 V, 5 mA g^{-1}) and opened in an argon-filled glove box. The cathodes were then removed from the coin cells and washed with DMC several times and allowed to dry. The cathodes were then wrapped in kapton tape and analyzed by XAS, transferred in a load-lock system for XPS analysis, or prepared in a glove box and transferred for microscopy analysis. For TEM sample preparation, the powders were suspended on a copper grid

with lacey carbon. The approximate time samples were exposed to air (from a sealed environment to the microscope column) was less than 5 seconds.

EELS/a-STEM

Electron microscopy work was carried out on a Cs-corrected FEI Titan 80/300 kV TEM/STEM microscope equipped with a Gatan Image Filter Quantum-865. All STEM images and EELS spectra were acquired at 300 kV and with a beam size of ~0.7 Å. EELS spectra shown in this work were acquired from a square area of ~0.5 × 0.5 nm with an acquisition time of 3 seconds and a collection angle of 35 mrad. HAADF images were obtained with a convergence angle of 30 mrad and a large inner collection angle of 65 mrad. Images acquired using an HAADF detector with a small convergence angle and a relatively large inner collection angle are also called "*Z*-contrast" images, where the contrast is proportional to $Z^{1.7}$.[10] In atomic resolution *Z*-contrast images, the contrast of the atomic columns thus can be used to differentiate different elements and provide atomic-structural information.

To minimize possible electron beam irradiation effects, EELS and HAADF figures presented in this work were acquired from areas without pre-beam irradiation. Mn L_3 to L_2 intensity ratio analysis was done by averaging over 8–11 spectra using the method described by Wang *et al.*[11]

X-ray photoelectron spectroscopy

X-ray photoelectron spectroscopy data were collected using a PHI 3056 spectrometer equipped with a hemispherical detector, 54.7 degrees off normal, with a dual Mg and Al anode source operated at 15 kV and an applied power of 350 W. The chamber pressure was kept at $<10^{-8}$ Torr during the measurements. High resolution data were collected at a pass energy of 5.85 eV with 0.05 eV step sizes and a minimum of 200 scans to improve the signal to noise ratio; lower resolution survey scans were collected at a pass energy of 93.5 eV with 0.5 eV step sizes and a minimum of 25 scans. The energy of the spectra was calibrated with the binding energy of the hydrocarbon C1s (C–H) at 284.6 eV, which corresponds mainly to the carbon black in the composite electrode and adventitious carbon. The data were analyzed using the software CasaXPS and all peaks were fit using a Shirley-type background.

X-ray absorption spectroscopy

XAS experiments were carried out at beamline X-11B at the National Synchrotron Light Source (NSLS) at Brookhaven National Laboratory. The incident beam was monochromatized using a channel-cut Si(111) monochromator detuned to 70% of the beam intensity at ~200 eV above either the Mn or Ni edge. Mn–K (~6539 eV) and Ni–K (~8333 eV) edge spectra were acquired in both transmission mode (T-XAS), utilizing a gas ionization chamber as a detector, and in total electron mode (TY-XAS) with helium gas flow. The setup is expressed graphically in Fig. 2.

Reference spectra of Mn and Ni foils were simultaneously collected for each edge and used to maintain energy calibration. X-ray absorption near edge structure (XANES) and extended X-ray absorption fine structure (EXAFS) data were analyzed using the Ifeffit and Horae packages.[12] The normalized k^3-weighted EXAFS spectra were Fourier transformed in a *k*-space of 2.5 to 7 $Å^{-1}$. Raw $\chi(k)$ data can be found in the ESI† (Fig. S5). EXAFS structural parameters were obtained using a nonlinear least squares analysis of the data using phase and amplitude functions generated from the FEFF6L code.[13] The least squares fits on the Fourier transforms were carried out with Ifeffit.

Results

Electrochemical properties

Electrochemical measurements of $Li[Li_{1/5}Ni_{1/5}Mn_{3/5}]O_2$ electrodes were performed in lithium half-cells. Fig. 3 displays the voltage

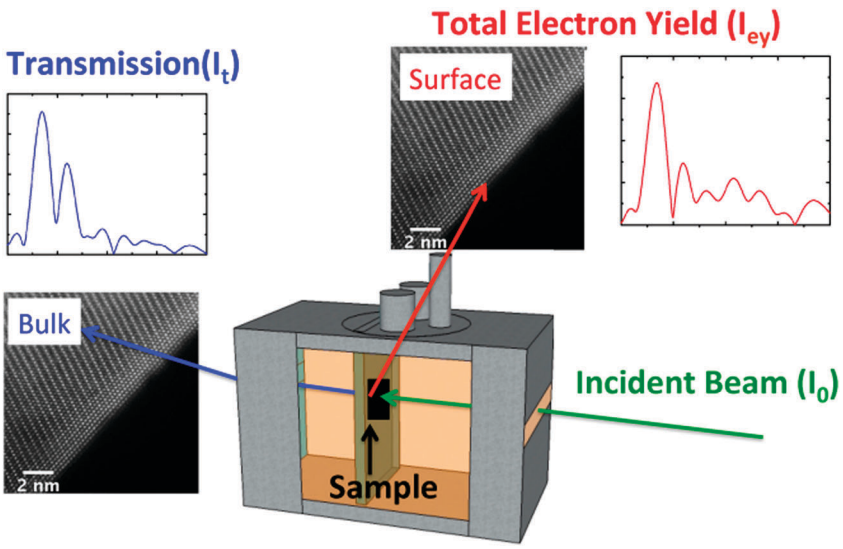

Fig. 2 Schematic showing the XAS setup used to run in both total electron yield and transmission mode, which was used to probe both the surface and bulk of the electrode material during cycling.

(*vs.* Li^+/Li^0) *versus* capacity (mA h g^{-1}) electrochemical curves in galvanostaic mode between 2.0 V and 4.8 V at a current density of 5 mA g^{-1} (C/50, C-rate). The points indicated along the charge and discharge profile correspond to cells that were stopped at various states of charge, disassembled in an argon-filled glove box, and prepared for characterization. Point A represents an uncharged pristine electrode, point B (at ~4.4 V) corresponds to the end of the sloped region and an extraction of ~110 mA h g^{-1} capacity, point C (at 4.45 V) corresponds to the beginning of the plateau region and an extraction of ~200 mA h g^{-1}, point D (at 4.60 V) corresponds to the middle of the plateau region and an extraction of ~220 mA h g^{-1}, point E (at 4.80 V) corresponds to a fully charged electrode and an extraction of ~300 mA h g^{-1} capacity. For the discharge points, point F (at 4.0 V) corresponds to ~50 mA h g^{-1} capacity, point G (at 3.30 V) corresponds to ~150 mA h g^{-1} capacity and lastly, point H (at 2.0 V) corresponds to a fully discharged electrode after one electrochemical cycle.

Structural and surface characterization using transmission electron microscopy (TEM) and electron energy loss spectroscopy (EELS)

Fig. 4 shows transmission electron microscopy images at various states of charge during the first electrochemical cycle as described in Fig. 3. It is worth noting that extreme effort was made to prevent prolonged air exposure before TEM characterization, which in our study was less than 5 seconds. The pristine electrode (Fig. 4A) shows a crystalline material with the layered ordering that extends to the surface of the particle.

After the sloped region (4.4 V), which corresponds to the Ni^{2+}/Ni^{4+} redox couple, the particles start to encounter high strain that results in a larger degree of defects and cracks when compared to the pristine material (Fig. 4B). Fell *et al.* recently used X-ray diffraction to quantify and explain the mechanism of these cracks as microstrain anomalies in the bulk of the $Li[Ni_xLi_{1/3-2x/3}Mn_{2/3-x/3}]O_2$ (x = 1/5) structure.[14] They showed that the microstrain originates from point defects, site-disorder, vacancies as well as plastic deformation. They also report that the microstrain originates from a Li deficient structure in the plateau region, however, there are multiple phenomena occurring in the bulk such as transition metal migration as well as oxygen loss, as this is where the largest degree of microstrain is observed. At the beginning of the discharge cycle, due to the presence of a larger degree of stacking faults within the structure, atomic resolution STEM imaging is not possible.

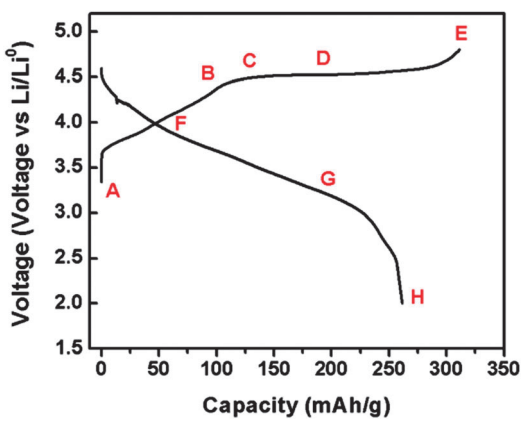

Fig. 3 First electrochemical charge/discharge curve between 2.0 V and 4.8 V (5 mA g^{-1}). The letter points indicate the states of charge where cells were prepared for characterization.

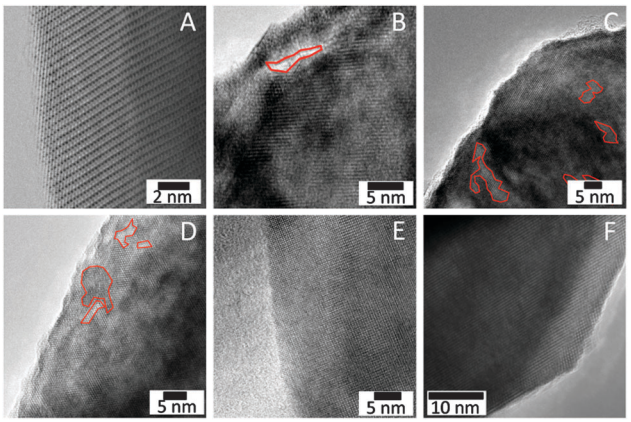

Fig. 4 TEM images for (a) pristine electrode material, (b) 4.4 V after the sloped region, (c) 4.45 V at the start of the plateau region, (d) 4.6 V at the middle of the plateau region, (e) 4.0 V at the first full charge, and (f) 2.0 V corresponding the first full electrochemical cycle.

Once the structure is re-lithiated, the crystal relaxes and atomic resolution STEM imaging is again possible. This continues until the particles are discharged completely to 2.0 V where the layered ordering reappears.

Fig. 5 compares the EELS spectra of the O–K and Mn–L edges from the *surface* of the crystal taken at different states of charge during electrochemical cycling. The structural evolution during the first electrochemical cycle can be interpreted using changes in the onset energy and the fine structures in the spectra. The intensities of all the spectra are normalized to the highest intensity peak. The onset energy of the O–K edge pre-peak is aligned to 532 eV. Therefore, our analysis of the O–K edge is limited to the fine structures and not to the chemical shift of the O–K edge. The Mn–L_3 and Mn–L_2 of transition metals are a result of the transition from $2p_{3/2}$ to $3d_{3/2}$, $3d_{5/2}$ and from $2p_{1/2}$ to $3d_{3/2}$, respectively. Their intensities are correlated to the unoccupied bands in 3d orbitals. Previous studies have shown that the L_3/L_2 ratio is sensitive to the valence state of Mn.[15]

Examining the Mn–L edge onset energy (Fig. 5a) during the sloping region of the first charging cycle shows that the peak shifts to a lower energy loss beginning at position C (4.45 V in Fig. 3), which may indicate a lower oxidation state. In the detailed L_3/L_2 ratio analysis shown in Fig. 5b, it is going to lower Mn oxidation state at point D, while points G and H are going back to higher Mn oxidation state, *i.e.* Mn^{4+}. It is worth mentioning here that the Mn oxidation state at point H does not fully return to Mn^{4+}.

Fig. 5c shows the O–K edge spectra. The splitting into two peaks for the O–K edge is a characteristic of the layered material. In the layered material, oxygen forms an O3 framework and the TM resides in octahedral sites. The crystal field of the TM splits

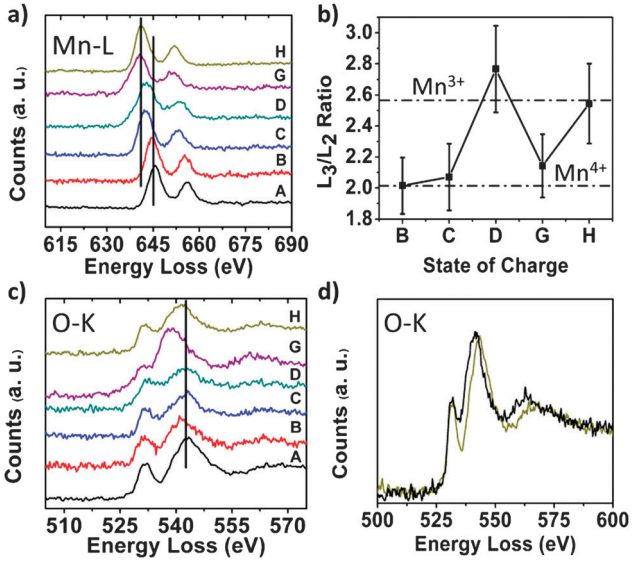

Fig. 5 Surface EELS data for the (a) Mn–L edge spectra, (b) Mn L_3/L_2 ratio fit results from the EELS spectra compared to literature values for various oxidation states of Mn species, (c) O–K edge spectra, and (d) comparison of the pristine and the fully discharged O–K edge.

into three t_{2g} orbitals at a lower energy and two e_g orbitals at a higher energy level. The K edge of oxygen is due to the transition of 1s electrons to the unoccupied 2p orbitals, which hybridized with the TM 3d orbitals. The splitting of the O–K-edge corresponds to the splitting of the TM 3d orbitals.

At positions C and D, the ratio of the first peak to the second peak increases, which may result from a larger amount of unoccupied t_{2g} orbitals of the neighboring TM ions and a change in the local environment of oxygen, such as bond length and oxygen vacancy formation. The increasing electron slots in t_{2g} orbitals can be from the oxidation of TM, *e.g.* Ni^{2+} to Ni^{4+}. The energy difference in the two peaks can also be an indication of the local environment change of oxygen. At point G, the ratio of the first peak to the second peak decreases, which is also consistently observed in the 2nd cycle (Fig. S1, ESI†), this is an indication of the reduction of TM ions, *i.e.* Ni^{4+} going back to Ni^{2+}. After one cycle, point H, the oxygen is not fully recovered to the original pristine state (Fig. 5d), which indicates that O and Mn are not fully reversible at the surface after the first electrochemical cycle.

Surface characterization using X-ray photoelectron spectroscopy (XPS)

X-ray photoelectron spectroscopy (XPS) was used to examine surface transformations at the cathode as a result of electrochemical cycling. We utilized a quasi *in situ* setup where samples were charged to points shown in Fig. 3, disassembled in an Argon-filled glove box and then transferred to the XPS using a custom designed transfer arm; this setup allowed for negligible air exposure. Fig. 6 shows the resulting XPS spectra for the C1s, O1s, Mn2p and Ni2p region scans at various points during the first electrochemical charge and discharge.

From the C1s, XPS spectra, the findings are summarized as follows. The C1s spectra show the presence of carbon black, the conductive agent used in the composite electrodes, and PVdF which is the polymeric binder. The P2p region scan (Fig. S2, ESI†) also shows the presence of only one peak that is attributed to the P in the $LiPF_6$ salt ($\sim$138 eV). During the first full electrochemical cycle there are no appreciable changes in the P2p spectra. However, changes in the F1s spectra (Fig. S2, ESI†) suggest that the

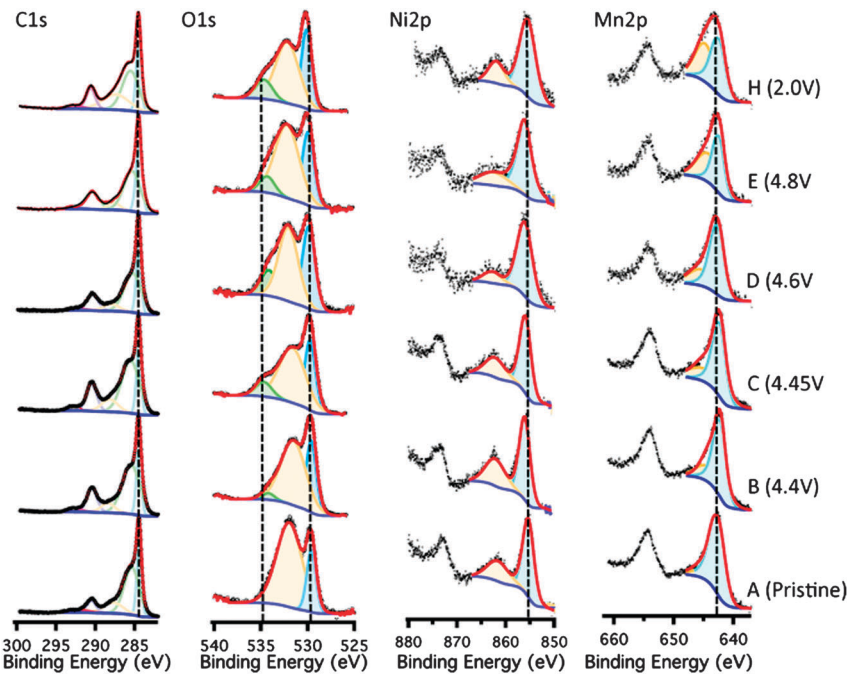

Fig. 6 XPS results for the C1s, O1s, Ni2p, Mn2p region scans during the first electrochemical cycle.

PVdF binder is undergoing some transformation as it shows the presence of two peaks attributing to PVdF and LiF starting at 4.6 V.

Since there is no visual change in the P2p region, it is believed that the LiF formation may not be a result of the decomposition of $LiPF_6$ ($LiPF_6 \rightarrow LiF + PF_5$), as the PF_5 would further react with any residual water to form POF_3, rather the formation of HF is thought to be a result of the dehydrofluorination of PVdF and subsequent reaction with LiF, occurring at room temperature.[9,16] However, reactions with $LiPF_6$ are also a likely source of the LiF.[17]

The O1s spectra show the presence of three main peaks. The first peak at 529.5 eV is commonly ascribed to the oxygen in the crystal lattice (O^{2-}). The second peak at ~532 eV (CO_3^{2-}) is associated with carbonate species as well as residual water or hydroxide on the surface of the particles. The ratio between the carbonate oxygen and the lattice oxygen remains fairly constant during the first cycle signifying only a small surface layer formation, however, a diminished intensity in the lattice oxygen and a subsequent increase in the carbonate oxygen during the second cycle reveals the formation of a surface layer is more significant after the first cycle.

In addition, a third peak forms inconsistently during the first and second cycle in the O1s region at a higher binding energy (~535 eV). The origin of this higher binding energy peak has been a subject of debate recently and a more detailed discussion of possible mechanisms are given below. One possible explanation of this peak in the literature is the formation of an oxygenated salt species, $Li_xPO_xF_y$ or $Li_xPF_YO_z$, from the hydrolysis of either $LiPF_6$ or PF_5 respectively.[18]

The Mn2p and Ni2p region scans can be summarized as follows. The pristine Ni2p shows a binding energy of ~855 eV, similar to published results.[19] After the sloped region, where the Ni^{2+}/Ni^{4+} redox occurs, the peak shifts to a higher binding energy of ~856.5 eV and remains unchanged when fully charged, suggesting that the nickel oxidation state change is complete after the sloped region. Upon discharge the peak shifts back to the Ni^{2+} oxidation state at 4.0 V and remains unchanged when fully discharged.

The Mn2p region scan shows a main peak at ~642 eV corresponding to Mn^{4+}.[20] No noticeable change is observed in the $Mn2p_{3/2}$ peak until 4.6 V where a noticeable broadening to higher binding energy occurs and increases until 4.8 V.

The observed broadening to higher binding energy may be a result of a higher valent Mn species, however, it may be a result of a F KL_1L_1 Auger overlap with the Mn2p which is common when using a Mg source (B.E. ~645 eV).[18b] To further investigate the Mn oxidation state during the first cycle, the Mn3p region was investigated. Utilizing the Mn2p and Mn3p regions allows one to probe both the surface layer (amorphous inner layer) (Mn2p) as well as the outer crystalline surface layer of the cathode material (Mn3p) by utilizing differences in the kinetic energy (Mn2p KE = 610 eV and Mn3p KE = 1204 eV) and escape depths, similar to reports on $LiCoO_2$.[21] Fig. 7 shows the Mn3p region scans for the pristine, 4.45 V, 4.8 V, and 2.0 V samples. The pristine material shows a main peak at 50.5 eV, which corresponds to Mn^{4+} and a second peak at 55 eV corresponding

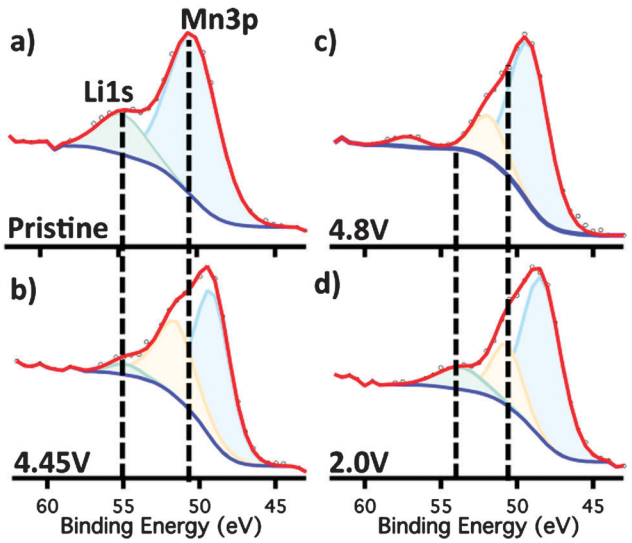

Fig. 7 Mn3p region scans for the (a) pristine electrode, and electrodes that were electrochemically charged to (b) 4.45 V, (c) 4.8 V, and (d) 2.0 V.

to Li 1s in the host structure.[22] At 4.4 V the Li1s peak disappears showing the movement of Li out of the host structure as well as a splitting in the Mn3p peak. The main peak shifts to a lower binding energy of ~48.8 eV, similar to Mn^{3+} in Mn_2O_3.[23] The fully charged sample (at 4.8V) shows the continued decrease of the Mn peak to ~48.5 eV, suggesting a Mn^{3+} species similar to Mn_3O_4.[23] After fully discharging the sample back to 2.0 V the Mn3p peak increases almost back to the original position at 48.8 eV, suggesting perhaps some Mn^{3+} still present and the Li1s peak at 55.5 eV returns. Furthermore, it is intriguing to see the Mn3p peak splitting (50.8 eV) during charging and this could be a result of a higher oxidation state formation at 4.4 V. However, when we ran a Mn^{7+} standard the peak was centered at 53.5 eV, much higher than the peak we observe.

As the Mn2p and Mn3p region scans suggest, during charging of the material after the $Ni^{2+/4+}$ redox, Mn may become electrochemically active. The Mn3p results are concurrent with the EELS data and show that the surface of the Li-excess material undergoes structural transformations, which result in the reduction of Mn whereas the Mn2p shows some broadening to higher binding energy suggesting the Mn is present in the outer amorphous layer and is oxidized above Mn^{4+}.

Local and electronic structure characterization using X-ray absorption spectroscopy (XAS)

X-ray absorption spectroscopy was used to study both the surface and bulk properties at the various states of charge in order to gain better insight into possible phase transformations during the first electrochemical cycle. We utilized both (T-XAS) as well as (TY-XAS) to monitor the K-edges of both Mn and Ni transition metals. TY-XAS is a surface sensitive technique, probing the top 5–15 nm of the particles surface, similar to that of the Mn3p XPS.[24] However, XPS is unable to give accurate transition metal structure and environment details, as the formed surface layer tends to make analysis convoluted. The ability to

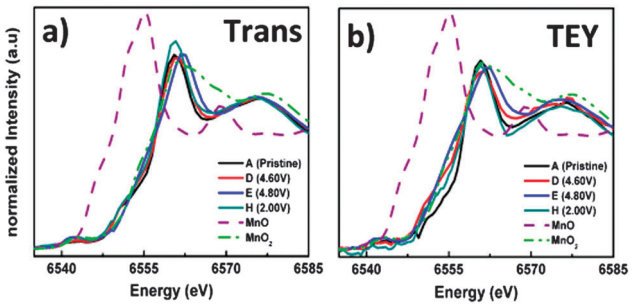

Fig. 8 Mn K-edge (a) transmission and (b) total electron yield XANES spectra during the first electrochemical cycle.

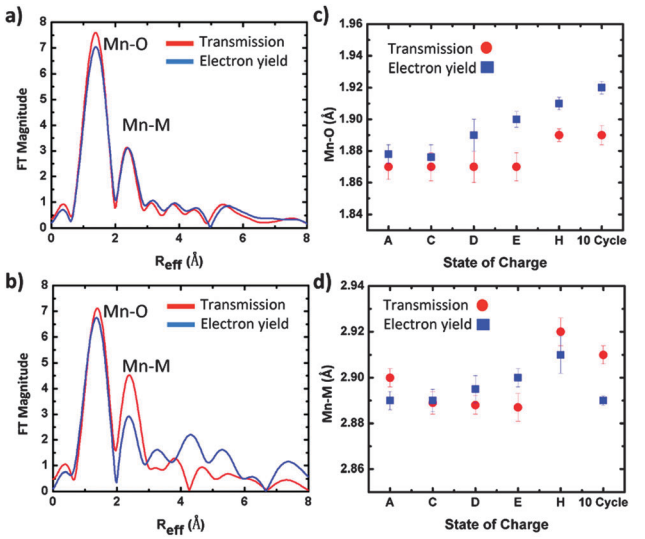

Fig. 9 k^3-weighted Fourier transform magnitudes of Mn K-edge spectra for transmission and total electron yield measurements on the (a) pristine and (b) discharged (2.0 V) cells and the curve-fitting results for (c) Mn–O and (d) Mn–M bond lengths *versus* different states of charge.

simultaneously probe the surface and bulk local and electronic structure of the material using X-ray absorption spectroscopy makes this setup unique. Fig. 8 shows the normalized XANES spectra of both the Mn–K T-XAS and TY-XAS. The Ni–K edge XANES spectra are shown in (Fig. S4, ESI†); for the pristine electrode the edge position is similar to reported values for Ni^{2+} in NiO.[16] A significant edge shift to higher energy is seen at 4.6 V and continues to push out to higher energy at 4.8 V which is likely a result of coordination effects rather than further oxidation. At 4.8 V the spectra are similar to that of Ni^{4+} species, as reported by others.[22c,6] Upon discharging the battery to 2.0 V, the oxidation state of Ni returns back to 2+, suggesting that a majority of the Ni redox reaction is reversible and little $Ni^{3+/4+}$ remains after the first cycle.

The simultaneous characterization of the Mn structure at the surface and bulk determined using T-XAS and TY-XAS was used to enhance the understanding of the observed changes seen in the EELS and XPS data. Fig. 8a and b show the Mn–K edge XANES spectra analyzed using T-XAS and TY-XAS, respectively. For each graph reference MnO and MnO_2 are shown which represent Mn^{2+} and Mn^{4+} oxidation states, respectively. As seen from the XANES spectra for both the bulk and the surface there are no noticeable oxidation state changes. The TY-XAS data, however, suggest that there is a slight shift to lower energy in the Mn–K edge position during cycling. However, the estimation of the oxidation state of Mn is not straightforward from just observing the XANES spectra as other factors, such as the local symmetry, can also change the shape of the XANES region.[25] In order to gain a better understanding of the Mn environment we analyzed the EXAFS region. Fig. 9a and b show two representative Fourier transform graphs comparing T-XAS and TY-XAS for a pristine and fully discharged (2.0 V) electrode, respectively. You can see from Fig. 9a that both the T-XAS and TY-XAS Fourier transforms for the pristine sample are closely related, providing evidence that the Mn–O and Mn–M bond lengths are similar in the bulk and the surface (Table S3, ESI†). Fig. 9b, however, exhibits a significant difference between the two spectra suggesting the occurrence of surface modulations after the first electrochemical cycle. Fig. 9c and d show the resultant EXAFS fits for the Mn–O and Mn–M bond lengths, respectively, for both T-XAS and TY-XAS. The analysis shows that the Mn–O and Mn–M bond lengths are similar for the un-cycled surface and bulk. However, after charging to 4.8 V, there is an increase in the Mn–O bond length as well as a decrease in the Mn–M bond length at the surface when compared to the bulk. The elongation of the Mn–O bond length in TY-XAS suggests a reduction of Mn at the surface of the crystal, as an increase in the ionic radii results in larger repulsion and subsequently a longer Mn–O bond (r Mn^{3+} = 0.65 Å, r Mn^{4+} = 0.53 Å).[25a,4c] The TY-XAS for the fully discharged sample (at 2.0 V) again shows a higher Mn–O bond length and even after the 10 electrochemical cycles this bond length remains higher than the pristine material signifying an irreversible Mn reduction at the surface of the crystal, while there are no significant changes in the bulk.

Discussion

Initial stage of lithium deintercalation (OCV to 4.40 V)

From the open circuit voltage to 4.40 V lithium is continually extracted from the material, shown visually as a sloped region in the electrochemical profile (Fig. 10). This region results in a capacity of roughly 110 mA h g^{-1} with the charge compensation resulting from the Ni (2+/4+) redox reaction, which is confirmed by our XPS, EELS and T-XAS results. In addition, our results show that both Mn and O in the structure remain unchanged to this point, with our T-XAS and TY-XAS data showing similar Mn–O and Mn–M bond lengths for the surface and bulk. Lastly, XPS analysis shows no major surface reactions for this region since there were no significant changes in the F1s, C1s, and P2p regions, which would be signified by the formation of phosphates and LiF, and carbonates, while the Mn3p region shows peak splitting, formation of lower oxidation state Mn, and lithium removal from the structure.

Plateau region (4.45 V to 4.8 V)

Following the sloped region, a plateau occurs from 4.45 V to 4.8 V and is associated with roughly 190 mA h g^{-1} of extra

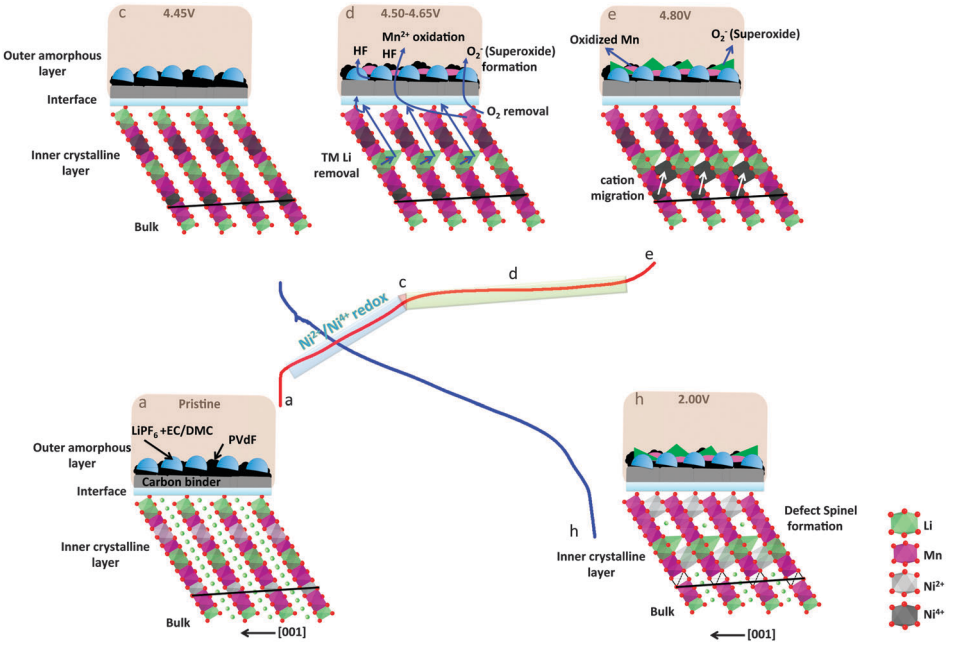

Fig. 10 Schematic showing the proposed mechanism for the formation and change in the electrode/electrolyte interface region during electrochemical cycling.

capacity. This region has been a focal point in the literature and attempts have been made to elucidate the origin of this anomalous capacity. Our EELS results show that the onset of the plateau (4.45 V) results in a shift in the Mn L_3/L_2 ratio signifying a slight reduction of the Mn. The Mn3p XPS region scan also shows a shift in the peak to lower binding energy confirming the presence of a reduced Mn. The result seems to be very counter-intuitive at first glance, as one would expect the oxidation of Mn if anything. However, the generation of the reduced Mn is a consequence of the formation of a large number of oxygen vacancies. Our preliminary first principles computational data indicate that the preferred charge compensation mechanism for oxygen vacancy formation is to have a neighboring transition metal with a reduced oxidation state (result not shown here).

The most noticeable change occurs at the middle of the plateau (4.60 V) with the EELS Mn L_3/L_2 ratio and the Mn3p XPS region showing the presence of Mn^{3+}. The EELS O–K spectra also show a decrease in the prepeak intensity. Xu *et al.* have previously explained the changes in the O–K prepeak signal as a distortion of the TM–O bonding, possibly from the weakening of the Mn–O bond caused by oxygen vacancy formation.[4b]

Oxygen vacancy formation

The charge compensation mechanism associated with this plateau region may be associated with oxygen vacancy formation and Mn reduction. To explore this in more depth, we examined the XPS O1s region. It is not until 4.45 V that we see the formation of a higher binding energy (535 eV) peak. While some reports show this peak attributed to the hydrolysis of $LiPF_6$ and PF_5 forming $Li_xPO_xF_y$ or $Li_xPF_YO_z$ species, we hypothesize in this work that this higher binding energy peak is associated with a superoxide species, which is similar to XPS studies by Lin *et al.* and Qui *et al.* who examined a variety of superoxide species.[26] Black *et al.* recently described in detail the formation mechanism for Li_2O_2/LiOH crystallization and the Li superoxide intermediate for Li–O_2 batteries.[27] Also, Laoire *et al.* described the reduction of oxygen in nonaqueous electrolytes *via* a one-electron process to form a superoxide.[28] It is also stated that the half-life of the superoxide is dependent on the nature of the electrolyte, in their case ionic liquids.

$$O_2 + e^- + Li^+ \rightarrow LiO_2 \quad (1)$$

$$LiO_2 + e^- + Li^+ \rightarrow Li_2O_2 \quad (2)$$

$$Li_2O_2 + 2e^- + 2Li^+ \rightarrow 2Li_2O \quad (3)$$

The reaction above is the proposed reduction of O_2 forming the LiO_2 superoxide radical which then reacts with Li to form Li_2O_2 on discharge, similar to reports by Yabuuchi *et al.*[16] Following this step, it is proposed that Li_2O_2 will again react with 2Li forming Li_2O. This has been confirmed in Li–O_2 battery systems by C and H NMR studies.[27] In addition, Black *et al.* have suggested that in the presence of MnO_2, PVdF, or Carbon-binder the formation of the superoxide radical occurs more abundantly.

We believe that the cause of the initial superoxide formation is the result of oxygen removal from the lattice and once at the surface of the crystal the oxygen reacts with the electrolyte and is reduced through an oxygen reduction reaction (ORR), similar to that seen in Li–O_2 batteries.[29] It has been shown that O_2 can react with ethylene carbonate (EC) and through a one-electron donation to the O_2 species cause a superoxide formation along with the decomposition of EC.[30] We believe that we are able to capture this superoxide species due to the unique nature of sample

preparation. Most XPS characterization requires the samples to be exposed to air for a certain duration and may result in the superoxide decomposition prior to analysis. For our measurements, however, the electrodes are never exposed to an ambient atmosphere, instead an Ar-atmosphere and a load-lock system are used to transfer the samples to the XPS. Furthermore, effort was taken in the preparation of the XPS samples to minimize time from galvanostatic cycling to XPS analysis. This could result in the analysis of a superoxide species, similar again to Qiu *et al.*[26b] This Li superoxide species remains throughout the plateau region and disappears during discharge. Examination of the 2nd electrochemical cycle reveals that the peak is only present during the first cycle.

Mn dissolution and subsequent oxidation

The Mn3p XPS and EELS data suggest that at the surface of the crystal Mn is reduced, causing changes in the Mn–O and Mn–M bonding. This is confirmed using TY-XAS by an elongated Mn–O bond, relative to the bulk. While we believe that some of the electrons from the formation of oxygen vacancies contribute to the anomalous capacity, we also believe that a portion of the electrons go towards reducing Mn. In addition, at these higher voltages, HF formation is known to occur through the deflourination of PVdF or $LiPF_6$.[9] The subsequent formation of HF coupled with the instability of the $Mn^{2+/3+}$ causes Mn to leach out of the structure and into the amorphous outer layer of the interface. At these higher voltages (4.6 V), Mn^{2+} can either be oxidized or react with fluorine to produce MnF_2, similar to that recently reported by Quinlan *et al.*[18b] However, after running MnF_2 and MnF_3 standards we do not believe this is the case for our system within the first and second electrochemical cycle.

From the first cycle XPS data, we can see a slight broadening in the Mn2p region scan, starting at 4.45 V. Also, HF formation causes the formation of LiF, which is slightly present at 4.40 V but more significant after 4.45 V in the F1s region. After the second complete electrochemical cycle, a full second peak appears at the higher binding energy.

Second cycle EELS at 4.45 V, 4.6 V and 2.0 V shows no change in the Mn. The EELS, TY-XAS, and XPS results suggest that all the Mn reactivity is limited to the first charge cycle, and relaxes during the first discharge. These results differ from the literature from Simonin *et al.*, which suggests the major reactions occur during the first discharge forming irreversible Li_2CO_3.[4c] On the basis of our results, we propose that the mechanism is largely attributed to oxygen vacancy formation. The oxygen vacancy formation coupled with the formation of HF causes the unstable $Mn^{2+/3+}$ to leach out of the crystal and into the outer surface layer where it is possibly oxidized. This outer surface layer creates a passivation layer. While second cycle EELS and XPS data still show changes in the oxygen, it is believed that this passivation layer suppresses (if not fully prevents) further Mn dissolution in subsequent cycles. With this in mind, our conclusion is that proper surface coating or activation of the surface of the Li-excess material would reduce these unwanted side reactions and first cycle capacity loss.

Conclusion

We examined the electrode/electrolyte interface of the lithium-excess nickel manganese layered oxide $Li_{1.2}Ni_{0.2}Mn_{0.6}O_2$ structure using X-ray photoelectron spectroscopy, X-ray absorption spectroscopy, and electron energy loss spectroscopy during the first two electrochemical cycles. Our results show the surprising reduction of Mn at the surface of the crystal accompanied by oxygen vacancy formation upon first charge. The resulting Mn on the surface of the crystal leaches out to the outer surface layer while lithium superoxide is converted to lithium peroxide. These reactions all occur at the first charge and result in the first cycle voltage plateau. We believe that further Mn dissolution is minimized during subsequent cycles as a result of the passivated surface layer. We also see strong evidence that O vacancy formation and recovery are largely reversible, though the exact mechanism remains to be explored.

Conflicts of interest

The authors declare no competing financial interest.

Acknowledgements

YSM, KJC, and DQ acknowledge the support from the Assistant Secretary for Energy Efficiency and Renewable Energy, Office of Vehicle Technologies of the U.S. Department of Energy under Contract No. DE-AC02-05CH11231, Subcontract No. 7056412 under the Batteries for Advanced Transportation Technologies (BATT) Program. GMV and LB acknowledge the support from the U.S. Department of Energy's Office of Basic Energy Science, Division of Materials Sciences and Engineering, under contract with UT-Battelle, LLC. KJC and SC acknowledge the use of the National Synchrotron Light Source, Brookhaven National Laboratory, supported by the U.S. Department of Energy, Office of Science, Office of Basic Energy Sciences, under contract no. DE-AC02-98CH10886. CRF acknowledges the financial support from Florida Energy System Consortium through University of Florida under Award Number 80859. We would like to thank Dr Nancy Dudney for invaluable discussions. DQ thanks Dr Huolin Xin for providing the scripts for Mn oxidation state analysis. a-S/TEM and EELS analysis were carried out at the ORNL Shared Research Equipment (SHaRE) User Facility, which is sponsored by the Office of Basic Energy Sciences, U.S. Department of Energy.

References

1 J. B. Goodenough and Y. Kim, *Chem. Mater.*, 2010, **3**, 587–603.
2 (*a*) C. S. Johnson, J. S. Kim, C. Lefief, N. Li, J. T. Vaughey and M. M. Thackeray, *Electrochem. Commun.*, 2004, **6**, 1085–1091; (*b*) J.-S. Kim, C. S. Johnson, J. T. Vaughey, M. M. Thackeray, S. A. Hackney, W. Yoon and C. P. Grey, *Chem. Mater.*, 2004, **16**, 1996–2006; (*c*) A. R. Armstrong, M. Holzapfel, P. Novak, C. S. Johnson, S.-H. Kang, M. M. Thackeray and P. G. Bruce, *J. Am. Chem. Soc.*, 2006, **128**, 8694–8698.

3 (*a*) N. Yabuuchi, K. Yoshii, S.-T. Myung, I. Nakai and S. Komaba, *J. Am. Chem. Soc.*, 2011, **133**, 4404–4419; (*b*) W.-S. Yoon, M. Balasubramanian, K. Y. Chung, X.-Q. Yang, J. McBreen, C. P. Grey and D. A. Fischer, *J. Am. Chem. Soc.*, 2005, **127**, 17479–17487; (*c*) A. R. Armstrong and P. G. Bruce, *J. Mater. Chem.*, 2005, **15**, 218–224; (*d*) A. R. Armstrong, A. D. Robertson and P. G. Bruce, *J. Power Sources*, 2005, **146**, 275–280; (*e*) Y. K. Sun, M. G. Kim, S. H. Kang and K. Amine, *J. Mater. Chem.*, 2003, **13**, 319–322; (*f*) S. H. Kang, Y. K. Sun and K. Amine, *Electrochem. Solid-State Lett.*, 2003, **6**, A183–A186.

4 (*a*) C. R. Fell, D. H. Lee, Y. S. Meng, J. M. Gallardo-Amores, E. Moran and M. E. Arroyo-de Dompablo, *Energy Environ. Sci.*, 2012, **5**, 6214–6224; (*b*) B. Xu, C. R. Fell, M. Chi and Y. S. Meng, *Energy Environ. Sci.*, 2011, **4**, 2223–2233; (*c*) L. Simonin, J.-F. Colin, V. Ranieri, E. Canevet, J.-F. Martin, C. Bourbon, C. Baehtz, P. Strobel, L. Daniel and S. Patoux, *J. Mater. Chem.*, 2012, **22**, 11316–11322; (*d*) Z. Lu and J. R. Dahn, *J. Electrochem. Soc.*, 2002, **149**, A815–A822; (*e*) A. D. Robertson and P. G. Bruce, *Electrochem. Solid-State Lett.*, 2004, **7**, A294–A298.

5 C. R. Fell, K. J. Carroll, M. Chi and Y. S. Meng, *J. Electrochem. Soc.*, 2010, **157**, A1202–A1211.

6 M. Jiang, B. Key, Y. S. Meng and C. P. Grey, *Chem. Mater.*, 2009, **21**, 2733–2745.

7 (*a*) S.-H. Kang and M. M. Thackeray, *J. Electrochem. Soc.*, 2008, **155**, A269–A275; (*b*) N. Tran, L. Croguennec, M. Menetrier, F. Weill, P. Biensan, C. Jordy and C. Delmas, *Chem. Mater.*, 2008, **20**, 4815–4825.

8 (*a*) R. Huang and Y. Ikuhara, *Curr. Opin. Solid State Mater. Sci.*, 2012, **16**, 31–38; (*b*) S. Zheng, R. Huang, Y. Makimura, Y. Ukyo, C. A. J. Fisher, T. Hirayama and Y. Ikuhara, *J. Electrochem. Soc.*, 2011, **158**, A357–A362; (*c*) R. Huang, Y. H. Ikuhara, T. Mizoguchi, S. D. Findlay, A. Kuwabara, C. A. J. Fisher, H. Moriwake, H. Oki, T. Hirayama and Y. Ikuhara, *Angew. Chem., Int. Ed.*, 2011, **50**, 3053–3057; (*d*) Y. Shao-Horn, L. Croguennec, C. Delmas, E. C. Nelson and M.A. O'Keefe, *Nat. Mater.*, 2003, **2**, 464–467.

9 K. Edström, T. Gustafsson and J. O. Thomas, *Electrochim. Acta*, 2004, **50**, 397–403.

10 (*a*) E. M. James and N. D. Browning, *Ultramicroscopy*, 1999, **78**, 125–139; (*b*) S. J. Pennycook, *Ultramicroscopy*, 1989, **30**, 58–69.

11 Z. L. Wang, J. Bentley and N. D. Evans, *Micron*, 2000, **31**, 355–362.

12 (*a*) J. J. Rehr and R. C. Albers, *Rev. Mod. Phys.*, 2000, **72**, 621–654; (*b*) J. J. Rehr, S. I. Zabinsky and R. C. Albers, *Phys. Rev. Lett.*, 1992, **69**, 3397–3400; (*c*) M. Newville, P. Livins, Y. Yacoby, J. J. Rehr and E. A. Stern, *Phys. Rev. B: Condens. Matter Mater. Phys.*, 1993, **47**, 14126–14131.

13 J. J. Rehr and R. C. Albers, *Rev. Mod. Phys.*, 2000, **72**, 621–654.

14 C. R. Fell, D. Qian, K. J. Carroll, M. Chi, J. L. Jones and Y. S. Meng, *Chem. Mater.*, 2013, **25**, 1621–1629.

15 (*a*) H. Kurata and C. Colliex, *Phys. Rev. B: Condens. Matter Mater. Phys.*, 1993, **48**, 2102–2108; (*b*) T. Riedl, T. Gemming and K. Wetzig, *Ultramicroscopy*, 2006, **106**, 284–291.

16 Y.-C. Lu, A. N. Mansour, N. Yabuuchi and Y. Shao-Horn, *Chem. Mater.*, 2009, **21**, 4408–4424.

17 (*a*) R. Sharabi, E. Markevich, K. Fridman, G. Gershinsky, G. Salitra, D. Aurbach, G. Semrau, M. A. Schmidt, N. Schall and C. Bruenig, *Electrochem. Commun.*, 2013, **28**, 20–23; (*b*) E. Markevich, R. Sharabi, H. Gottlieb, V. Borgel, K. Fridman, G. Salitra, D. Aurbach, G. Semrau, M. A. Schmidt, N. Schall and C. Bruenig, *Electrochem. Commun.*, 2012, **15**, 22–25.

18 (*a*) M. Herstedt, M. Stjerndahl, A. Nytén, T. Gustafsson, H. Rensmo, H. Siegbahn, N. Ravet, M. Armand, J. O. Thomas and K. Edström, *Electrochem. Solid-State Lett.*, 2003, **6**, A202–A206; (*b*) R. A. Quinlan, Y.-C. Lu, Y. Shao-Horn and A. N. Mansour, *J. Electrochem. Soc.*, 2013, **160**, A669–A677; (*c*) A. M. Andersson, D. P. Abraham, R. Haasch, S. MacLaren, J. Liu and K. Amine, *J. Electrochem. Soc.*, 2002, **149**, A1358–A1369.

19 (*a*) K. M. Shaju, G. V. Subba Rao and B. V. R. Chowdari, *Electrochim. Acta*, 2004, **49**, 1565–1576; (*b*) K. M. Shaju, G. V. S. Rao and B. V. R. Chowdari, *J. Electrochem. Soc.*, 2004, **151**, A1324–A1332; (*c*) K. M. Shaju, G. V. S. Rao and B. V. R. Chowdari, *J. Electrochem. Soc.*, 2003, **150**, A1–A13; (*d*) K. Amine, H. Tukamoto, H. Yasuda and Y. Fujita, *J. Power Sources*, 1997, **68**, 604–608; (*e*) K. Amine, H. Tukamoto, H. Yasuda and Y. Fujita, *J. Electrochem. Soc.*, 1996, **143**, 1607–1613.

20 (*a*) K. M. Shaju, G. V. Subba Rao and B. V. R. Chowdari, *Electrochim. Acta*, 2002, **48**, 145–151; (*b*) K. M. Shaju, G. V. Subba Rao and B. V. R. Chowdari, *Electrochem. Commun.*, 2002, **4**, 633–638.

21 L. Dahéron, R. Dedryvère, H. Martinez, M. Ménétrier, C. Denage, C. Delmas and D. Gonbeau, *Chem. Mater.*, 2007, **20**, 583–590.

22 (*a*) T. Eriksson, T. Gustafsson and J. O. Thomas, *Electrochem. Solid-State Lett.*, 2002, **5**, A35–A38; (*b*) T. Eriksson, A. M. Andersson, A. G. Bishop, C. Gejke, T. Gustafsson and J. O. Thomas, *J. Electrochem. Soc.*, 2002, **149**, A69–A78; (*c*) W.-S. Yoon, C. P. Grey, M. Balasubramanian, X.-Q. Yang and J. McBreen, *Chem. Mater.*, 2003, **15**, 3161–3169; (*d*) W. S. Yoon, N. Kim, X. Q. Yang, J. McBreen and C. P. Grey, *J. Power Sources*, 2003, **119**, 649–653; (*e*) M. Sathiya, K. Ramesha, G. Rousse, D. Foix, D. Gonbeau, A. S. Prakash, M. L. Doublet, K. Hemalatha and J. M. Tarascon, *Chem. Mater.*, 2013, **25**, 1121–1131.

23 M. Oku, K. Hirokawa and S. Ikeda, *J. Electron Spectrosc. Relat. Phenom.*, 1975, **7**, 465–473.

24 S. L. M. Schroeder, *Solid State Commun.*, 1996, **98**, 405–409.

25 (*a*) A. R. Jaszewski, R. Stranger and R. J. Pace, *Phys. Chem. Chem. Phys.*, 2009, **11**, 5634–5642; (*b*) B. Gilbert, B. H. Frazer, A. Belz, P. G. Conrad, K. H. Nealson, D. Haskel, J. C. Lang, G. Srajer and G. De Stasio, *J. Phys. Chem. A*, 2003, **107**, 2839–2847.

26 (*a*) C. L. Lin, S. L. Qiu, J. Chen, J. M. Tranquada, M. Strongin, J. E. Crow and C. W. Chu, *Phys. C*, 1989, **162–164**(Part 2),

1325–1326; (*b*) S. L. Qiu, C. L. Lin, J. Chen and M. Strongin, *J. Vac. Sci. Technol., A*, 1990, **8**, 2595–2598.

27 R. W. Black, S. H. Oh, J.-H. Lee, T. Yim, B. Adams and L. F. Nazar, *J. Am. Chem. Soc.*, 2012, **134**, 2902–2905.

28 (*a*) C. O. Laoire, S. Mukerjee, K. M. Abraham, E. J. Plichta and M. A. Hendrickson, *J. Phys. Chem. C*, 2009, **113**, 20127–20134; (*b*) C. O. Laoire, S. Mukerjee, K. M. Abraham, E. J. Plichta and M. A. Hendrickson, *J. Phys. Chem. C*, 2010, **114**, 9178–9186.

29 (*a*) Y.-C. Lu, D. G. Kwabi, K. P. C. Yao, J. R. Harding, J. Zhou, L. Zuin and Y. Shao-Horn, *Energy Environ. Sci.*, 2011, **4**, 2999–3007; (*b*) N. Yabuuchi, Y.-C. Lu, A. N. Mansour, T. Kawaguchi and Y. Shao-Horn, *Electrochem. Solid-State Lett.*, 2010, **13**, A158–A161; (*c*) G. M. Veith, N. J. Dudney, J. Howe and J. Nanda, *J. Phys. Chem. C*, 2011, **115**, 14325–14333.

30 L. Xing, W. Li, C. Wang, F. Gu, M. Xu, C. Tan and J. Yi, *J. Phys. Chem. B*, 2009, **113**, 16596–16602.

